CrossMark

Experimental and numerical analyses on the effect of stiffness on bedded sandstone strain burst with varying dip angle

Manchao He[1] · Fuqiang Ren[1,2] · Cheng Cheng[3]

Abstract

Strain burst violence is related to the stiffness ratio (SR) between environmental and bursting rock masses. Strain burst tests on dolomite specimens with different system stiffnesses and bedded sandstone with four different dip angles as well as numerical analyses of strain burst with different structures are carried out to study the effect of stiffness on strain burst. Results indicate that strain burst intensity is larger in a more flexible system environment, and lower SR corresponds to a larger probability of strain burst. Additionally, with increasing SR, the failure mode becomes more stable, and the influence of the structures on failure mode vanishes gradually. For the lowest SR, the strain energy densities (SEDs) from the surrounding rock are lower for steep structures, while flatter structures correspond to higher SED. Moreover, for vertical and horizontal structures, variation in SED with SR is more sensitive; however, for steep and medium discontinuities, the sensitivity is lower.

Introduction

Strain burst is commonly a violent rock failure closely related to the excavation of brittle rock (Hoek 2008), and copious amounts of research (Hucka and Das 1974; Singh 1988; Andreev 1995; Zhang et al. 2011) has focused on the mechanical behavior of the rock material as well as brittleness. However, brittleness does not completely describe the nature of strain burst, and other factors likely help determine the energy release in strain burst (Hoek 2008).

Rock burst could be regarded as a stability problem similar to the behavior of a rock specimen in a laboratory test (Cook 1965), i.e., whether the specimen will fail violently or not depends on the relative stiffness between the sample and loading system. Based on the complete stress-strain curve obtained by the stiff test machine (Salamon 1970), the relationship between specimen stability and system stiffness was discussed in the perspective of energy and equilibrium in detail. If a rock structure is stiffer than the loading system (Blake 1972), more energy can be applied to the structure, causing rock burst upon fialure. The system stiffness, stress level, and released energy are three important parameters that must be considered together to assess unstable rock failure (Brady and Brown 1981; Kaiser et al. 1996; Kaiser and Tang 1998; Aglawe 1999; Stavrogin et al. 2001; Hedley 2002).

Brady and Brown (1981) studied the stability of pillars with different width-to-height ratios and different stope spans based on boundary element analysis. Kaiser and Tang (1998) used rock failure process analysis (RFPA) models to study the failure process, stress-strain response, seismic events, and seismic energy release during uniaxial compression tests and pillar failure in the field considering different system stiffnesses. Three different numerical tools were employed to carry out uniaxial compression tests with variable platen stiffness and obtain the corresponding system responses, including the stress-strain behavior of the specimen and loading system (Kias et al. 2011).

The theory based on system stiffness helps us understand more about the strain burst mechanism; however, to date, practical application in the field due has been difficult due to complex geological conditions. Because the rock mass always contains some fractures or other structural planes, the strength of the rock

✉ Fuqiang Ren
renfuqiangcumtb@163.com

1   State Key Laboratory for Geomechanics & Deep Underground
     Engineering, Beijing 100083, China

2   School of Mechanics and Civil Engineering, China University of
     Mining & Technology, Beijing 100083, China

3   Institute of Geology and Geophysics Chinese Academy of Science,
     Beijing 100029, China

Fig. 1 Photograph showing the elements of the strain burst main machine (He et al. 2010)
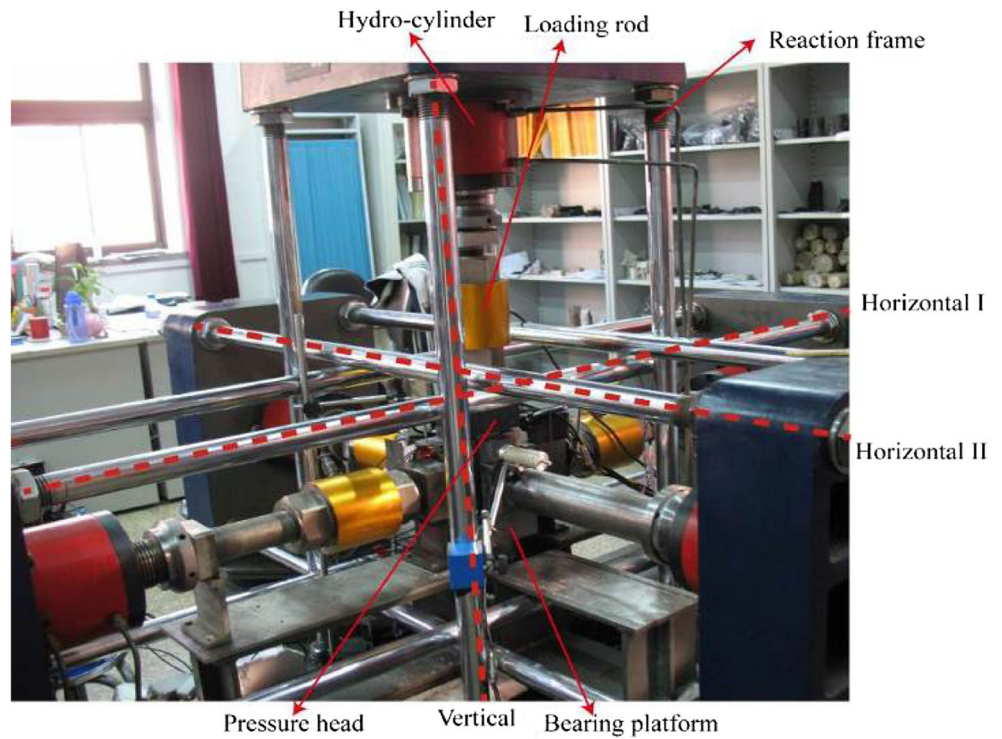
mass can only determine whether a failure will happen instead of how violent the failure will be. Moreover, laboratory strain burst tests (He et al. 2012b) have proved that the orientation of structural planes has an influence on strain burst; however, this influence will not be investigated in this contribution.

The stiffness ratio (SR) between the environment and the bursting rock mass is a key factor influencing failure mode

and violence. However, the effect of stiffness on strain burst has not been experimentally studied under true tri-axial stress conditions, and the effect of rock mass structure on SR has not been studied systematically. The stiffness effect of strain burst was studied qualitatively; moreover, strain burst tests for sandstone with different dip angles were conducted to study the effect of varying bedding dip angle on stiffness. Numerical
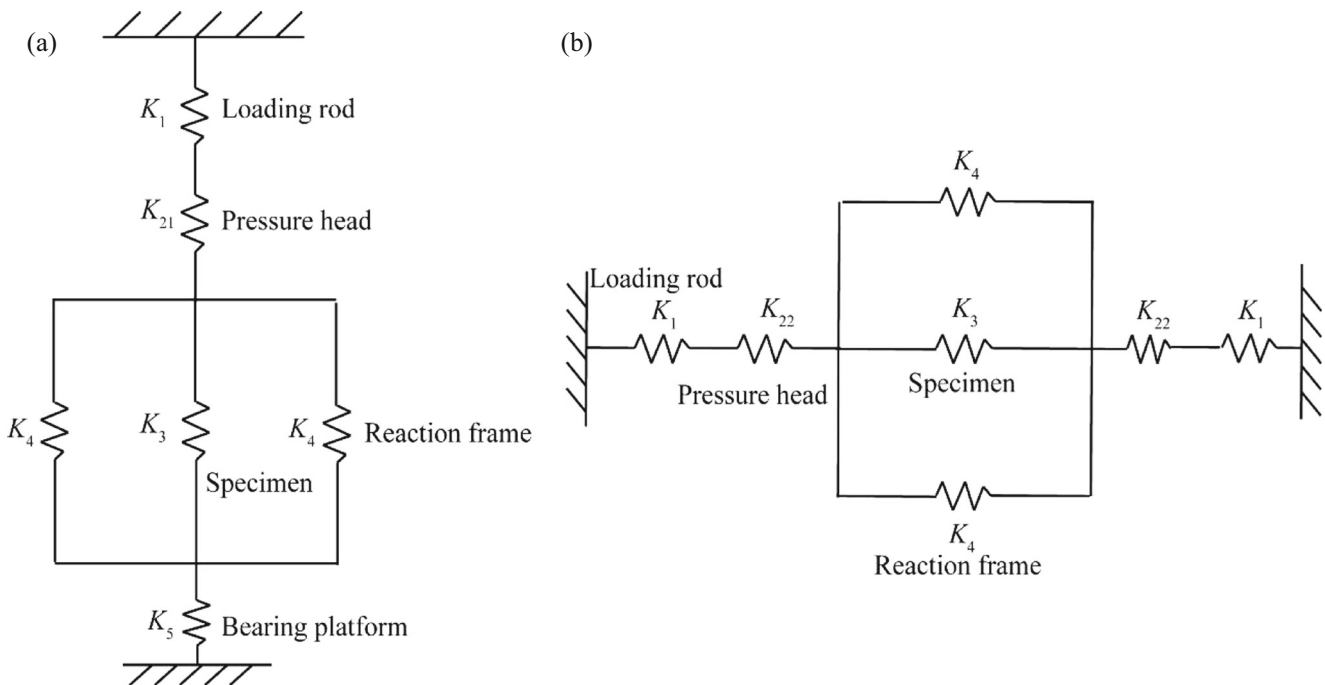

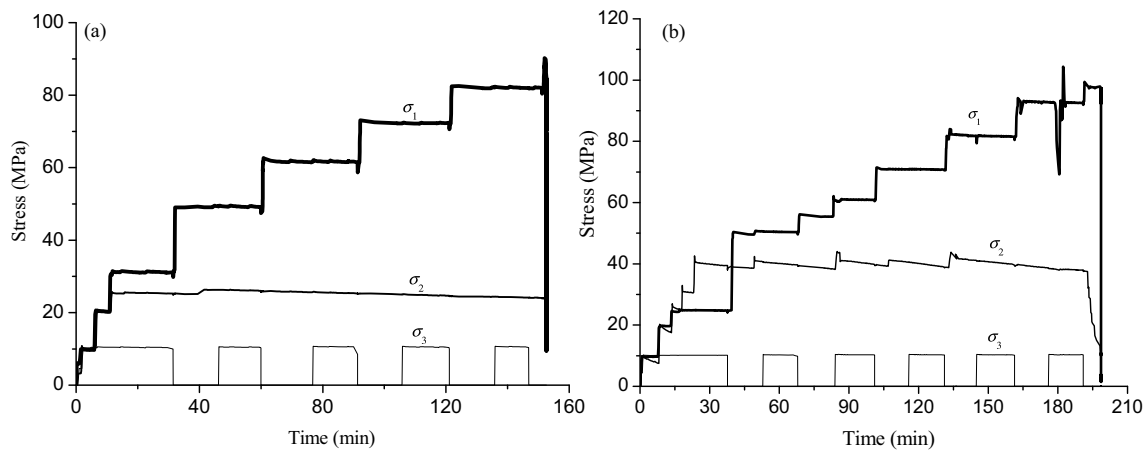Fig. 2 Schematic of the stiffness calculation, (a) vertical and (b) horizontal I direction

Fig. 3 Stress paths for strain burst tests, (a) specimens Y1 and (b) Y2

analysis was used to systematically study the effect of structure-related stiffness on strain burst.

Effect of stiffness on strain burst

Stiffness of the experimental system

Laboratory strain burst experiments are conducted using the deep rock burst test system (He et al. 2010) developed at the China University of Mining and Technology, Beijing. This experimental system is composed of the main machine, hydraulic control system, and data acquisition equipment (Fig. 1). The deep rock burst test system is a true tri-axial compressive apparatus in which one surface of the prismatic specimen can be unloaded abruptly to simulate excavation in the field, allowing this system to reproduce strain burst in the laboratory (He et al. 2012a).

The main elements of the strain burst machine are the reaction frame, hydro-cylinder, loading rod, pressure head, and the bearing platform in a vertical direction. Figure 2 shows the connections of the elements in vertical and horizontal I directions. For the vertical direction, the

Fig. 4 Strain burst ejection process and failure state for (a) specimens Y1 and (b) Y2
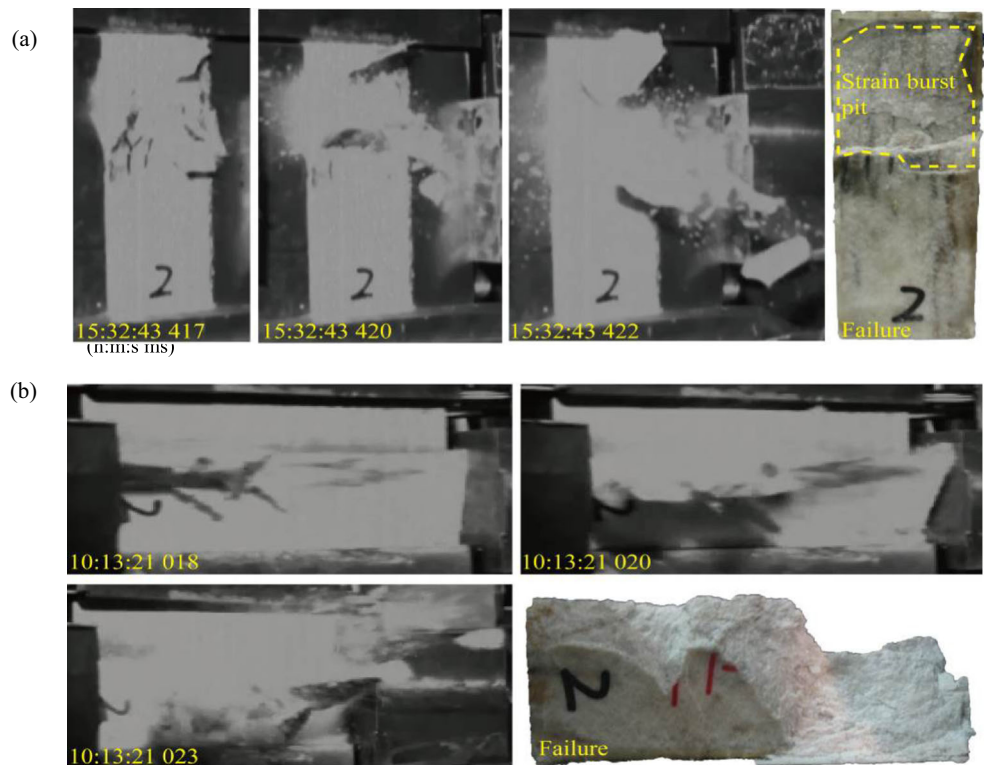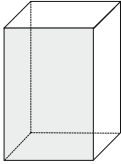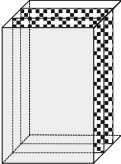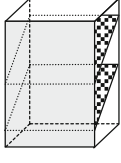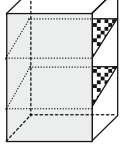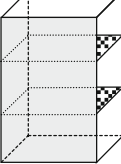
Table 1 Physical and mechanical parameters of sandstone samples and failure stress state

Specimen	Dip angle (°)	Sketch of specimen*	UCS (MPa)	Young's modulus (GPa)	SR	Initial stress state (MPa)	Failure stress state (MPa)		
							σ_1	σ_2	σ_3
S	/		127.6	38.6	/	/		/	
S0	0		112.1	37.6	1.80		130.4	30.6	0.0
S30	30		63.8	33.5	2.02		114.3	29.5	0.0
S60	60		105.6	34.9	1.93	$\sigma_1=35.7$ $\sigma_2=30.0$ $\sigma_3=22.1$	125.4	34.6	0.0
S90	90		121.2	39.1	1.73		137.3	33.7	0.0

*The shadow represents the bedding plane and the gray face represents the unloading face

reaction frame and specimen are connected in parallel; additionally, they are both connected to the hydro-cylinder, loading rod, pressure head, and bearing platform in series. The element stiffness can be calculated by Eq. (1). In addition, Eqs. (2) and (3) are the formulas for the system stiffness whose elements are connected in series and parallel, respectively.

$$K = \frac{AE}{l} \tag{1}$$

$$K_{\text{series}} = \frac{1}{\frac{1}{K_1} + \frac{1}{K_2} + \dots + \frac{1}{K_n}} \tag{2}$$

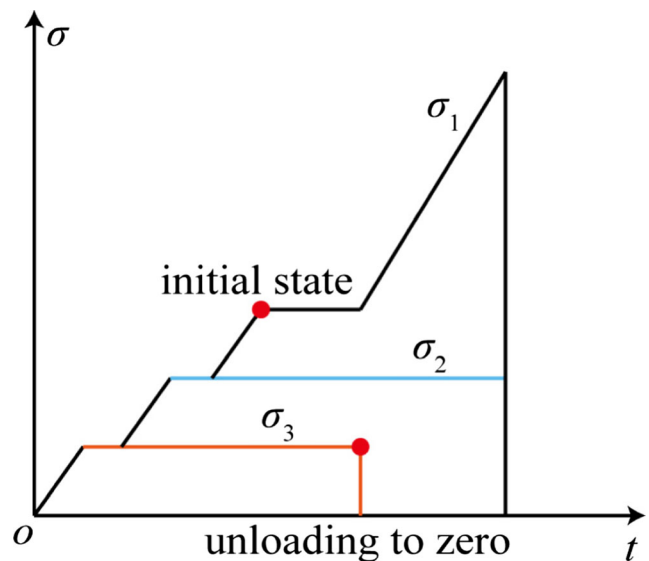$$K_{\text{parallel}} = K_1 + K_2 + \dots + K_n \tag{3}$$

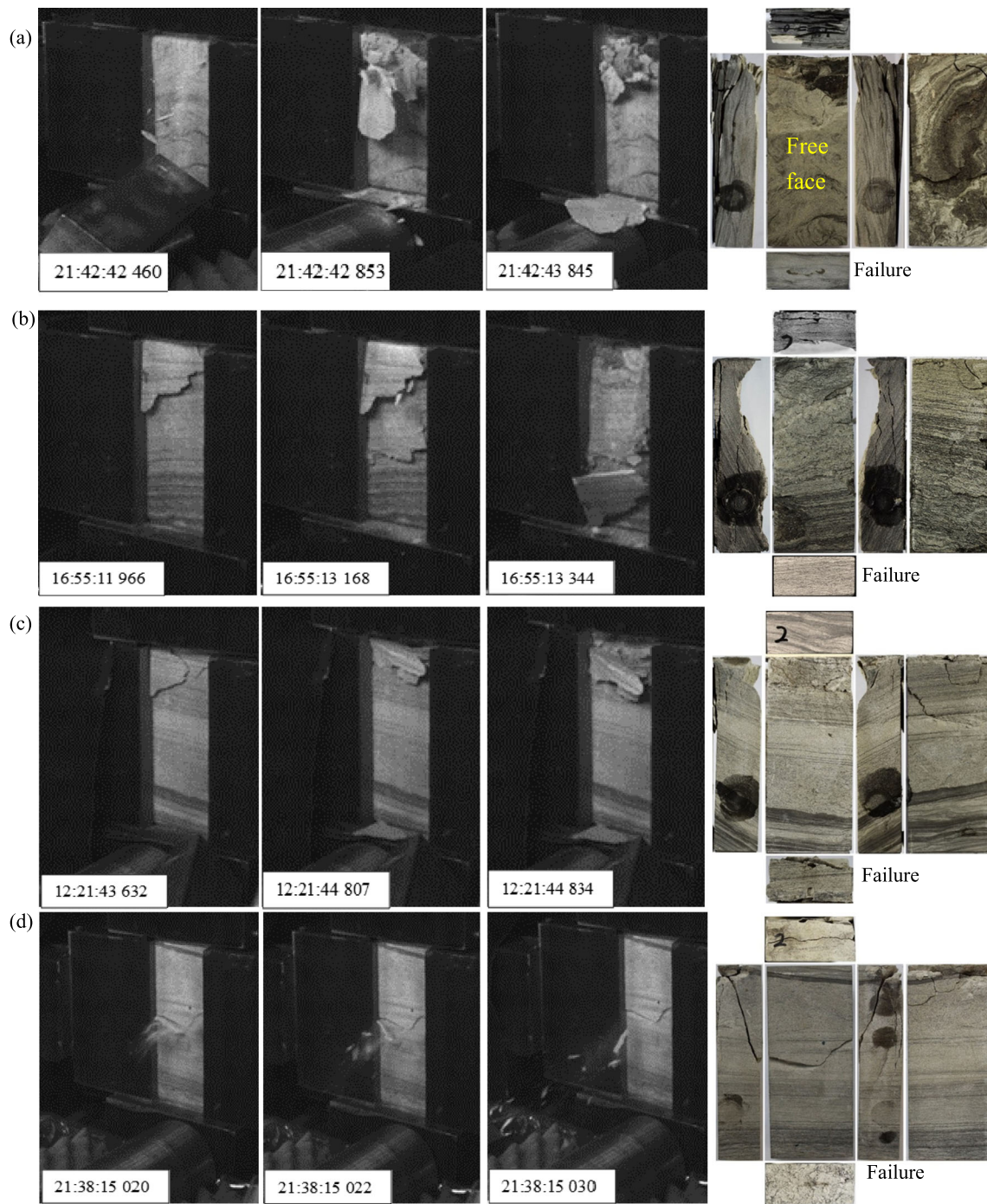**Fig. 5** Stress path of sandstone strain burst

Fig. 6 Failure process of sandstone strain burst. Dip angles are (a) 0°, (b) 30°, (c) 60°, and (d) 90°

where K is the stiffness, A is the cross-sectional area of element, E is Young's modulus, and l and n are the length and number of elements, respectively. During the stiffness calculation, the hydro-cylinder was omitted because of complications. The original purpose was to distinguish the system stiffness in the vertical and horizontal directions. Hence, the stiffnesses of the experimental system in the vertical and horizontal I directions are 0.54 GN/m and 0.32 GN/m, respectively.

Verification of the effect of stiffness on strain burst

Dolomite was used to conduct strain burst tests utilizing different machine stiffnesses in the vertical and horizontal I directions. The dolomite was collected from a deep tunnel in TengChong, YunNan province. Samples have the nominal dimensions of $150 \times 60 \times 30$ mm. Specimens were loaded in a true triaxial stress state and then one side was unloaded suddenly to simulate excavation. Simultaneously, the vertical
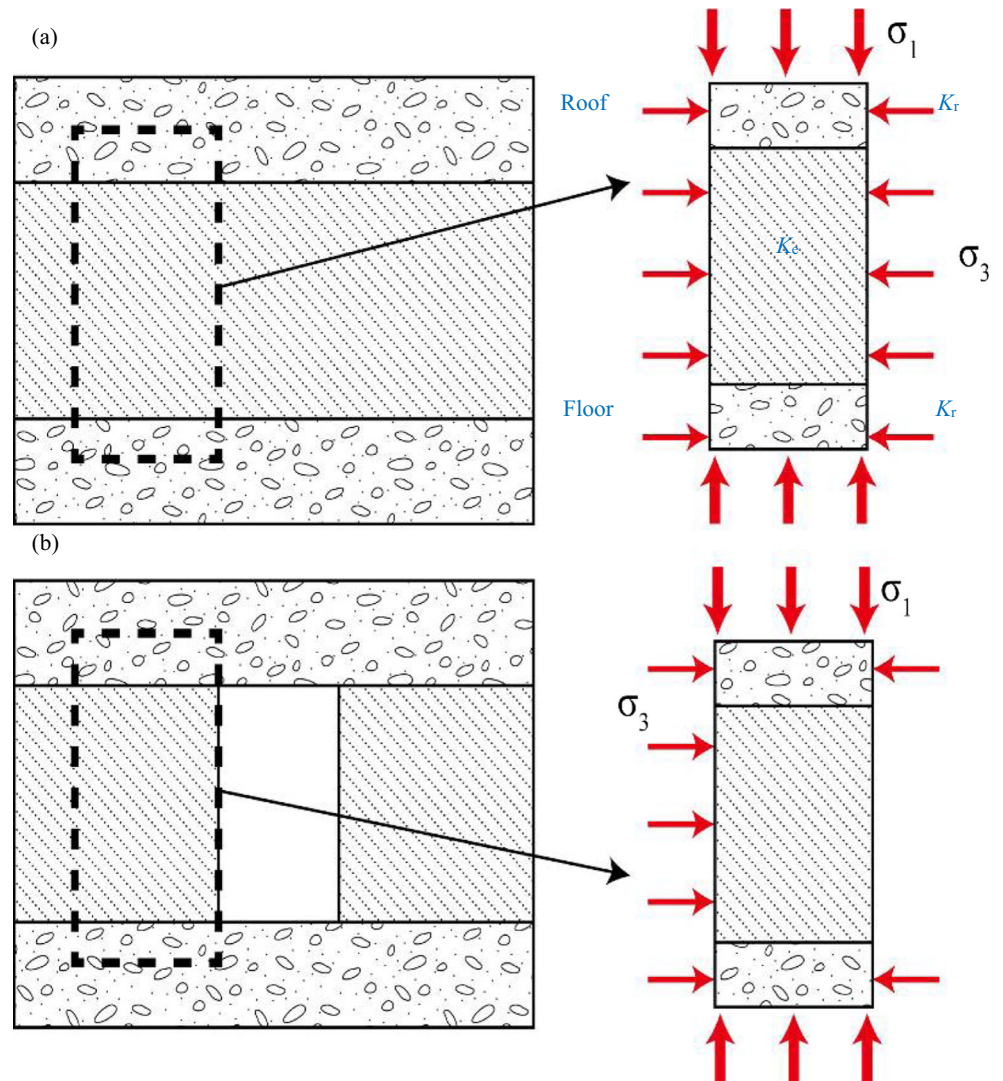
stress was increased to simulate stress concentration due to the opening. If failure did not occur in 15 min after unloading, the unloaded surface was reloaded and the sample was placed in a higher true triaxial stress state and held for another 15 min. The process of unloading and reloading was repeated until failure.

Figure 3 shows the stress paths of the two tests. The maximum principal stress (σ_1) of specimen Y1 was loaded in the vertical direction while specimen Y2 was loaded in the horizontal I direction. At failure, σ_1 was 90.3 MPa and 98.1 MPa for specimens Y1 and Y2, respectively. The SR can be defined as Eq. (4); so, the SR of Y2 is smaller than that of Y1.

$$SR = \frac{K_{\text{machine}}}{K_{\text{specimen}}} \tag{4}$$

Figure 4 Shows the ejection process captured by high-speed camera and the failure state after testing. The ejection for Y2 was more violent and the strain burst pit was larger than

Y1; i.e. the strain burst intensity of specimen Y2 was larger, which corresponds to the lower SR. In other words, the intensity of strain burst is larger in a more flexible system.

Effect of stiffness on sandstone strain burst with varying dip angle

The influence of experimental system stiffness in different direction to strain burst was studied in "Verification of the effect of stiffness on strain burst" Section. In this section, some strain burst experiments on sandstone are carried out to study the effect of stiffness on sandstone strain burst with varying bedding plane dip angle.

Sandstone specimens were collected from the NingTiaoTa coal mine, Shanxi province, and the sampling depth was about 800 m. The samples had dimensions of $100 \times 40 \times 20$ mm.

Table 1 shows the physical and mechanical parameters of sandstone samples with four different dip angles (0°, 30°, 60°, and 90°). During strain burst testing, the dip direction was

Fig. 8 Numerical model for strain burst, (a) before and (b) after excavation (*Note that the different colors only mark the distribution of structural planes instead of different layers with various properties)
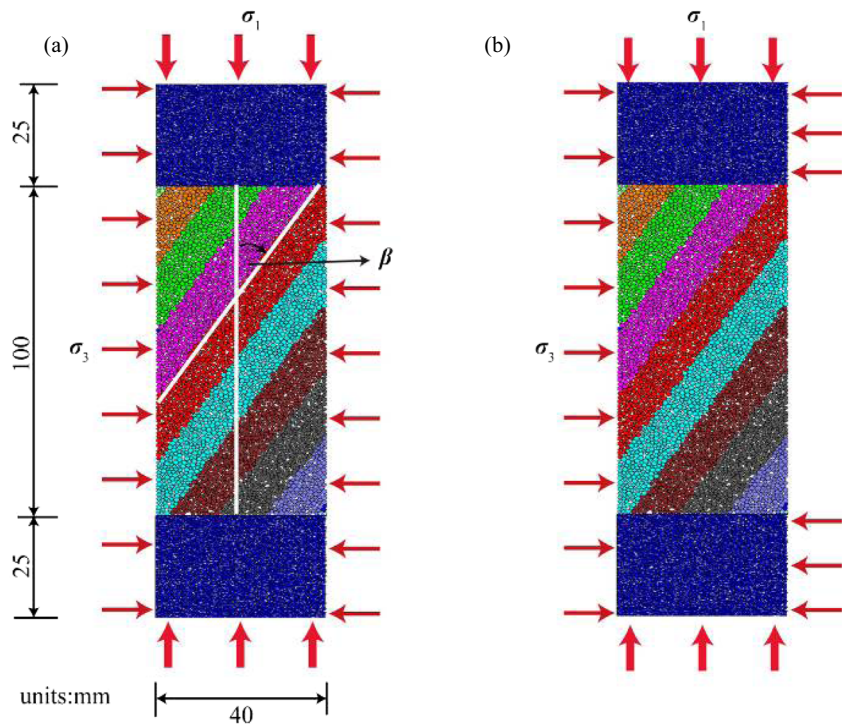
always toward the unloading face. Additionally, uniaxial compression tests were carried out to obtain the essential mechanical parameters of the sandstone. The mean uniaxial compression strength (UCS) of a similar sandstone (collected from same roadway) with no visible bedding was 127.6 MPa. When the dip angle was 60°, the UCS (63.8 MPa) was minimal. Additionally, the UCS (112.1 MPa, 63.8 MPa, 105.6 MPa, and 121.2 MPa) and Young's modulus for different dip angles (from 0° to 90°) first decreased and then increased (when the angle was 90°, reaching the maximum with all values being smaller than those for intact sandstone). Moreover, the SRs of the four specimens were calculated using Eq. (4). The maximum SR (2.02) corresponds to a dip angle of 30°, and when the dip angle equals 90°, the value of SR (1.73) is minimal.

Figure 5 shows the stress path of the sandstone. The initial stress was identified according to the fitted general far-field stress relationship at depth for North China (Tan 1995). Using a mining depth of 1170 m (which is the designed mining

depth, in the future), we obtain the initial stress of $\sigma_1 =$ 35.7 MPa, $\sigma_2 = 30.0$ MPa, and $\sigma_3 = 22.1$ MPa. Additionally, the initial stress was loaded gradually to keep the experimental system stable and keep the stress uniform. However, in the numerical analysis, the loading time is unnecessary. When the initial stress state was held for 10 min, σ_3 was unloaded to zero and σ_1 was loaded to 0.25 MPa/s until strain burst occurred. The failure stress state is listed in Table 1; the variation in σ_1 failure relative to the four different dip angles was similar to the UCS in that it decreased firstly and then increased.

Figure 6 shows the failure process for sandstone strain burst tests. Fragment ejection was observed when the dip angle was 0° and 90° (Fig. 6a and d), and ejection intensity was stronger in the latter. When the dip angle was 30° and 60°, there was no obvious fragment ejection. Spalling and splitting were the major failure modes. In addition, the spalling area for the specimen with a 30° dip angle was larger than that for a 60° dip. Table 1 shows the SR values. The minimal SR (1.73, specimen S90) corresponds to the

Table 2 Micro-parameters of the numerical model

	E_c, $\overline{E}_c$ (GPa)	k_n/k_s, $\overline{k}_n/\overline{k}_s$	$\overline{\sigma}_n$ (MPa)	$\overline{\sigma}_s$ (MPa)	R_{min} (mm)	R_{max}/R_{min}	$\overline{\lambda}$	μ
Excavation body	48	6.0	110 ± 27.5	110 ± 27.5	0.42	1.66	1.0	0.5
Roof and floor	0.3, 1, 10, 100	6.0	1,000,000 ± 0	1,000,000 ± 0	0.42	1.66	1.0	0.5

Note: E_c and $\overline{E}_c$ are the contact modulus and parallel bond modulus, respectively; k_n/k_s and $\overline{k}_n/\overline{k}_s$ are the contact SR (normal to shear) and parallel bond SR (normal to shear), respectively; $\overline{\sigma}_n$ is the parallel normal bond strength, while $\overline{\sigma}_s$ is the parallel shear bond strength; μ is the coefficient of friction; R_{min} is the minimum particle radius, and R_{max}/R_{min} is the particle radius ratio (maximum to minimum); $\overline{\lambda}$ is the parallel bond radius ratio (defined as R_{bond}/R_{min})

Fig. 9 The (a) calibration model and (b) corresponding stress-strain curve
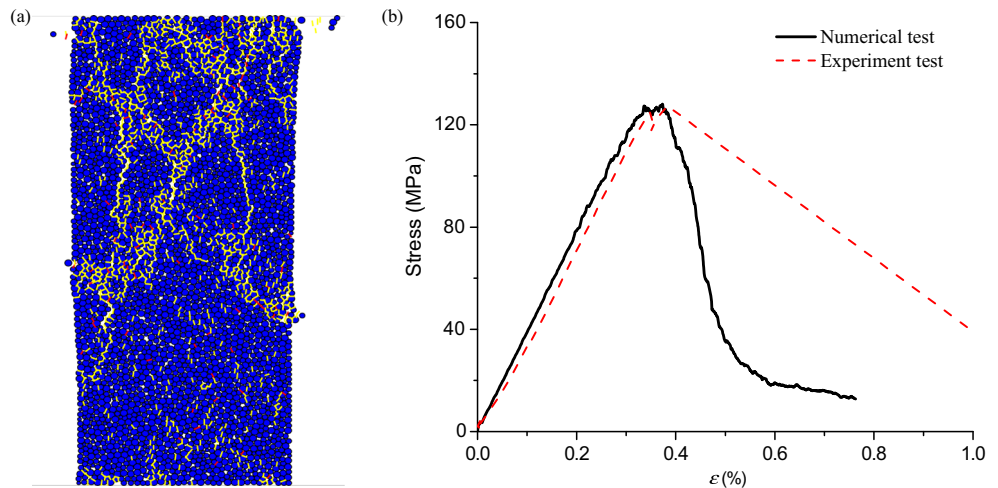
most obvious ejection, while the largest SR (2.02, specimen S30) corresponds to spalling failure.

Experimental results prove that the SR of the experimental machine and the specimen is a key factor influencing the violence of strain burst. In addition, strain bursts occurring in roadways and tunnels are always controlled by the orientation of bedding or structural planes (Ortlepp and Stacey 1994). The SR is possibly the internal reason for this phenomenon.

Numerical tests for bedded sandstone with different dip angles

A series of numerical tests using particle flow code (PFC) are described in this section. The numerical analysis is a supplement to the experiments, because sandstone sample processing is difficult due to breakage along bedding planes. Additionally, the numerical tests avoid the influence of sample heterogeneity.

Geomechanical model

Commonly, the surrounding rock mass near an underground opening may contain several different types of strata with various stiffnesses (Fig. 7). During excavation and stress redistribution in the surrounding rock mass, different amounts of strain energy will be stored and then released when the rock mass fails, which can lead to distinct types of failure around the opening. In addition, the different orientation of structural planes in a rock mass may also induce a different failure mode.

In Fig. 7, it is assumed that the roof and floor have the same stiffness K_r, and the rock to be excavated has the stiffness K_e. Similar to Eq. (4), the SR can be expressed as:

$$SR = \frac{K_r}{K_e} \qquad (5)$$

Theoretically, SR may influence the energy release and violence of failure after excavation. The K_e changes with different orientations of the structural plane. In this plane strain problem, the rock mass containing various rock strata suffers vertical and horizontal stress before excavation, and the horizontal stress on one side of a rock stratum is removed to simulate excavation, while both the roof and floor are confined.

Numerical model

Based on the geomechanical model, the bonded particle model was built to analyze the effect of SR on strain burst. Figure 8 shows the numerical model for strain burst. Two particle assemblies with a size of 40×25 mm simulating the roof and floor are built at the top and bottom of the 40×100-mm model excavation wall. In this model, β (from 0° to 180° with an interval of 15°) is defined as the angle from the vertical line to the structural planes. The numerical models with different structure orientation have different Young's moduli, so the stiffness (K_e) and SR are also different. The Young's moduli were calculated according to the uniaxial compression test for the numerical model (40×100 mm).

Micro-parameters

The numerical tests focus on the influence of dip angle on stiffness of the excavation body (K_e), so, other parameters are held constant. In the roof and floor models, the normal

Table 3 Parameters for the structural plane model

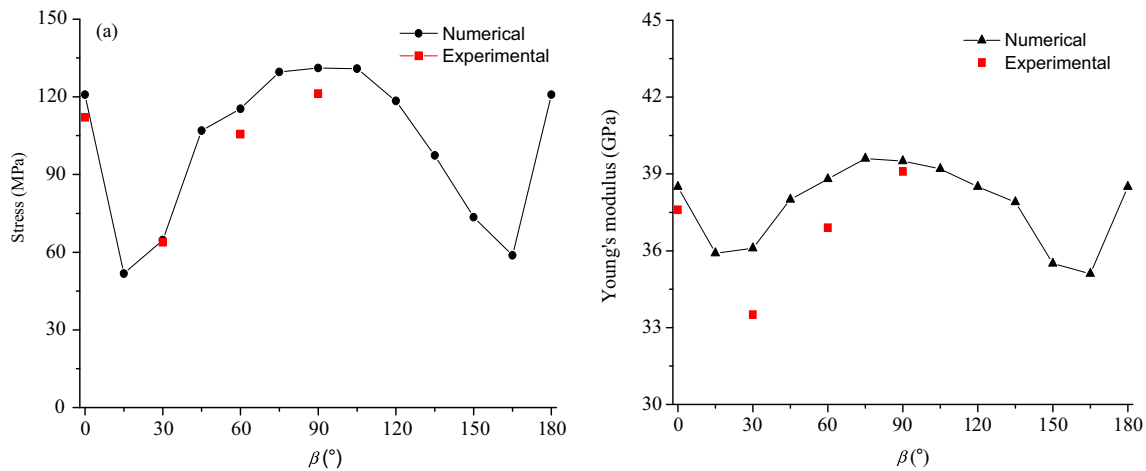| dip	[0°, 180°], with an interval of 15°
origin	(0, 0)
spacing	10 mm
fric	0.5
n_bond, s_bond	0 MPa

Fig. 10 Relationship between (a) UCS, (b) Young's modulus, and structural plane orientations

and shear bond strengths between the grains are set quite high to guarantee that failure only occurs in the excavation body. The micro-parameters of the roof and floor in the strain burst model are listed in Table 2.

A model (without structural planes) with dimensions of 40×100 mm was built and calibrated according to the physical and mechanical parameters of the sandstone (without bedding planes, specimen S, in Table 1). The mechanical parameters of sandstone with different bedding plane orientations are controlled by the structure, which leads to changes in micro-parameters. In this section, the dip angle is the unique variable and other parameters are kept constant. Hence, the micro-parameters of the particle were determined by testing intact sandstone, and those parameters are constant in the numerical tests.

In particular, some key micro-parameters (E_c, $\overline{E}_c$, $\overline{\sigma}_n$ and $\overline{\sigma}_s$) were adjusted to fit the experimental results. Additionally, other parameters were selected according to the Kulatilake et al. (2015). Fig. 9 shows the calibration model, corresponding stress-strain curve, and experimental results. The calibrated micro-properties are presented in Table 2.

The interfaces between the roof/floor and the excavation body use a joint model with a frictional coefficient of 0 and cohesion of 0 (Cho et al. 2007); however, interfaces are not absolutely smooth due to the roughness of the models.

Table 3 lists the micro-properties of the structural planes in the models. Additionally, the "origin" identifies the position of the discontinuities, and "fric" gives the friction coefficient of the balls at the surface of each of the planes. In this study, "fric" (0.5) was designed according to Kulatilake et al. (2015). Moreover, "spacing" is defined as the distance between two neighboring structural planes. "n_bond" and "s_bond" determine the normal and shear strength of the planes, respectively. The "spacing", "n_bond", and "s_bond" were set to 10 mm, 0 MPa, and 0 MPa, respectively. The influence of the bond strength, coefficient of friction, and spacing will be discussed in "Discussion" Section.

Figure 10 gives the numerical and experimental results for UCS and Young's modulus of the rock mass with different structural orientations. Young's modulus will be used to calculate the stiffness and obtain the SR value. Moreover, the variation in UCS for different dip angles is similar to Tien (2006), which proves the reasonability of the numerical model and micro-parameters. The rock mass has the highest UCS and Young's modulus when the structural planes are horizontal or vertical. However, if β is 15° or 165°, the values of UCS and Young's modulus are lowest.

Loading path

Figure 11 shows the loading path for the strain burst numerical test. The initial stress was $\sigma_1 = 35.7$ MPa, $\sigma_2 = 30.0$ MPa, and $\sigma_3 = 22.1$ MPa. We assume that σ_2 is parallel to the opening direction. In the PFC model, the in-situ stress state was applied biaxially (σ_1 and σ_3 in the two-dimensional model) with a loading rate of 0.05 m/s. After removing the horizontal stress
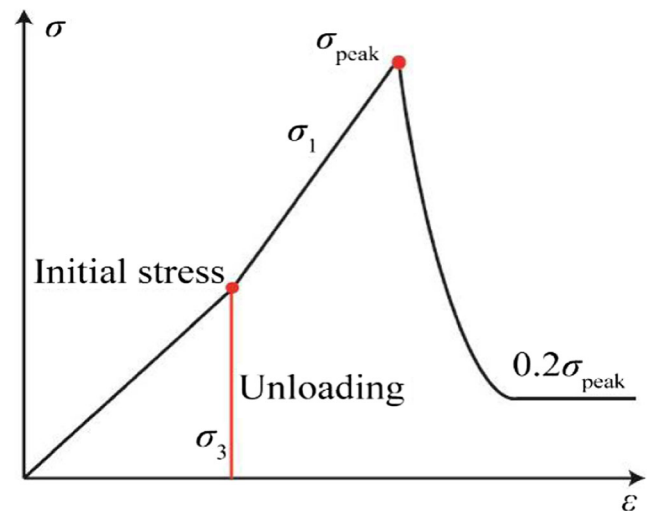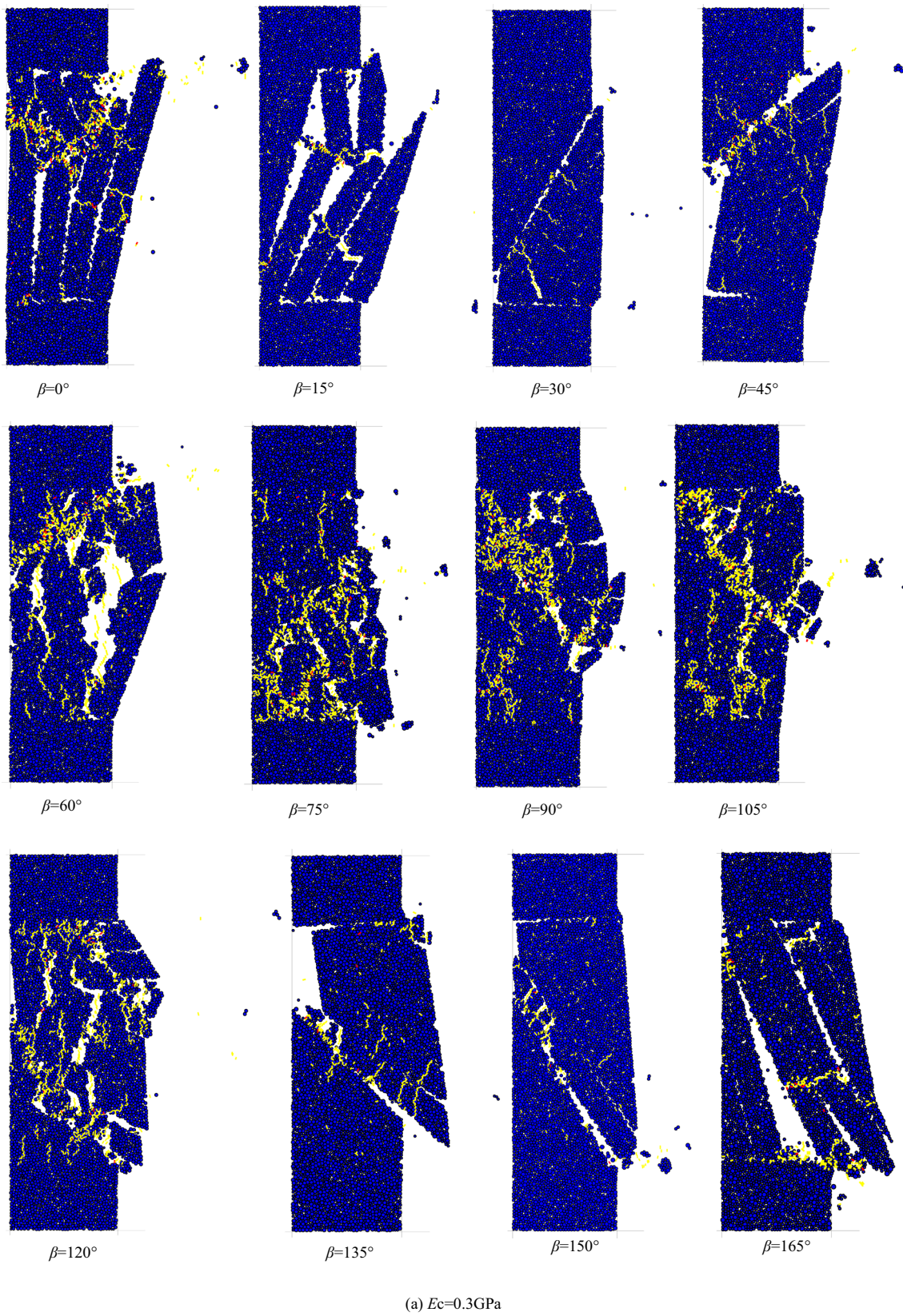

Fig. 11 Strain burst loading path

$\beta=0°$ $\beta=15°$ $\beta=30°$ $\beta=45°$
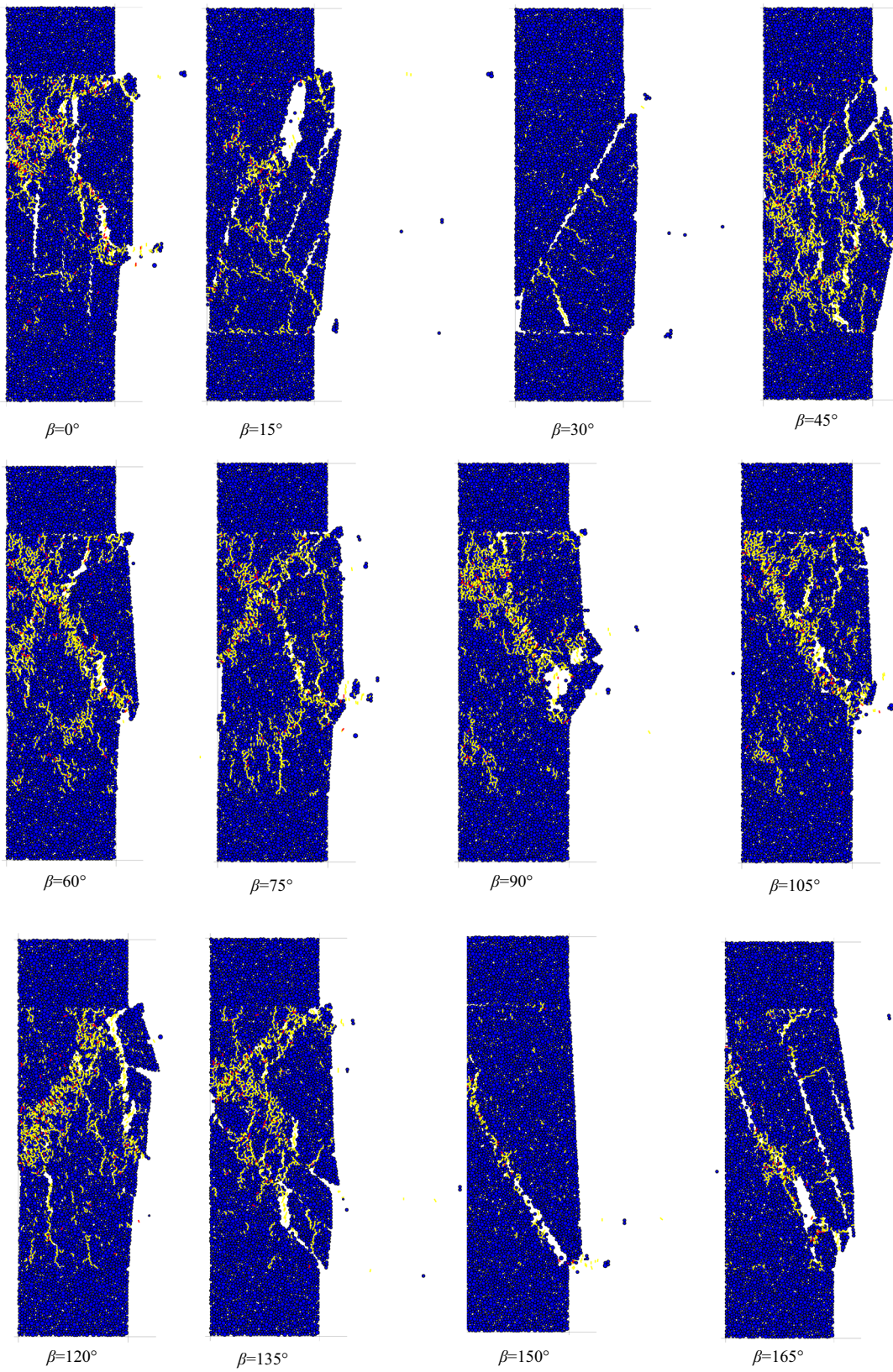
$\beta=60°$ $\beta=75°$ $\beta=90°$ $\beta=105°$

$\beta=120°$ $\beta=135°$ $\beta=150°$ $\beta=165°$

(a) E_c=0.3GPa

Fig. 12 Deformation features of the rock mass with different structural plane orientations

β=0° β=15° β=30° β=45°

β=60° β=75° β=90° β=105°

β=120° β=135° β=150° β=165°

(b) E_c =1GPa

Fig. 12 (continued)

$\beta=0°$ $\beta=15°$ $\beta=30°$ $\beta=45°$ $\beta=60°$ $\beta=75°$

$\beta=90°$ $\beta=105°$ $\beta=120°$ $\beta=135°$ $\beta=150°$ $\beta=165°$
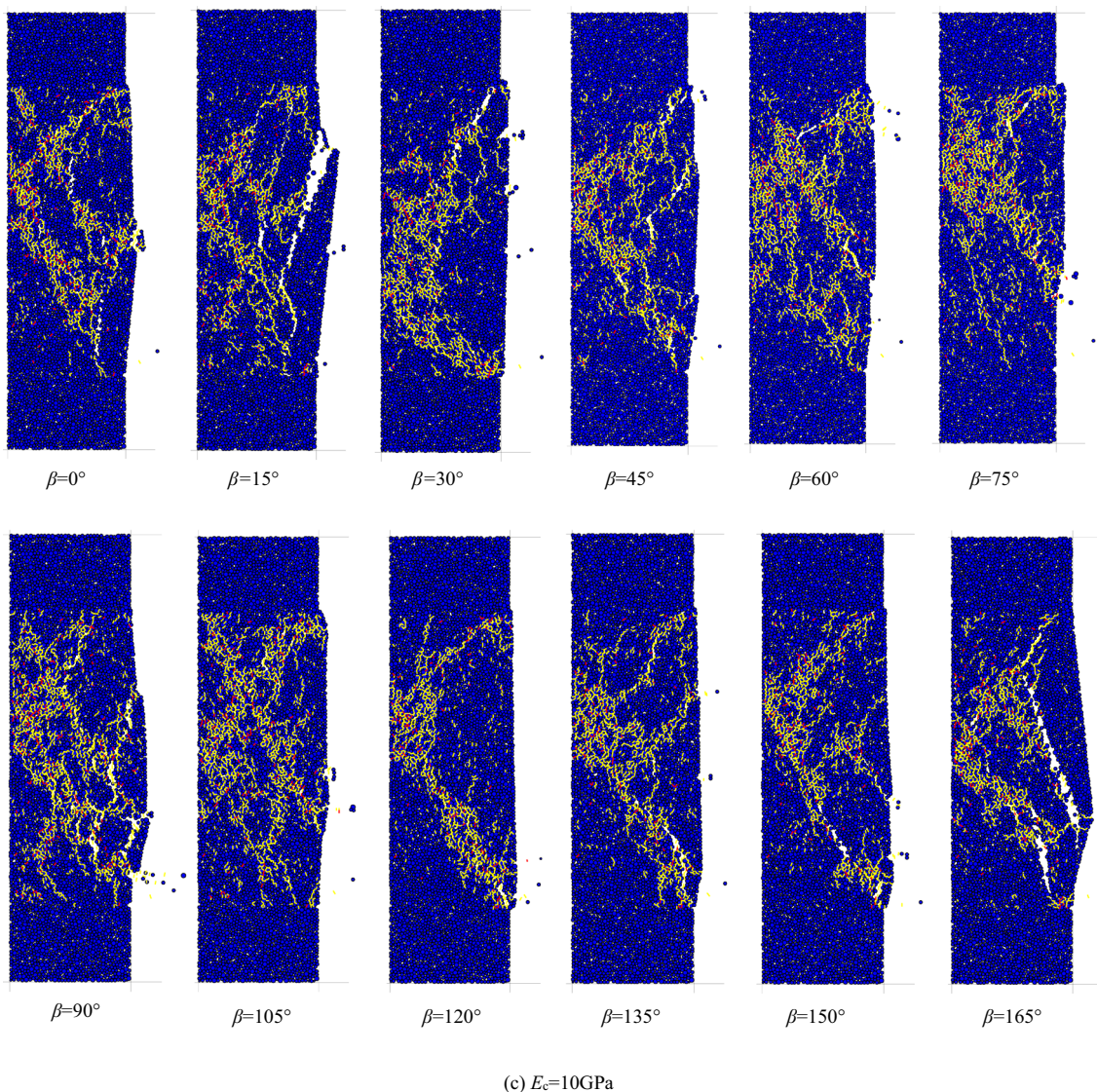
(c) E_c=10GPa

Fig. 12 (continued)

from one side, which simulates excavation, stress will concentrate in the vertical direction. The rate of concentration rate is set to be 0.2 m/s. In addition, tests were terminated when the σ reached 20% of σ_{peak}.

Analysis results

Failure characteristics

Five groups of numerical analyses were carried out to study the effect of structure-related stiffness on strain burst. In each test group, the surrounding rock mass (roof and floor) has the same properties, while the bursting rock mass has structural planes varying in β angle from 0° to 180° at an interval of 15°. For different test groups, the roof and floor have different parallel bond moduli and contact moduli (E_c), including 0.3 GPa, 1 GPa, 10 GPa, and 100 GPa, which is a micro-property of the model and can influence the stiffness of the roof and floor.

Figure 12(a) shows the results of the numerical analysis when $E_c = 0.3$GPa. Tensile failure occurs along the structural planes and buckling with particle and fragment ejection at $\beta = 0°$ (180°). Tensile failure with some sliding along structural planes and buckling forms at $\beta = 15°$, and the main failure mode was sliding along structural planes at $\beta = 30°$ and 45°. At $\beta = 60°$, in additional to a shear failure along structural planes, vertical tensile failure occurred in the rock mass and violent buckling occurred close to the unloading surface with some fragment ejection. At $\beta = 75°$ or 90°, the main failure mode was tensile failure. When β varies from 105° or 165°, the structures are similar to 75° to 15°, and the failure modes are also almost symmetrical.
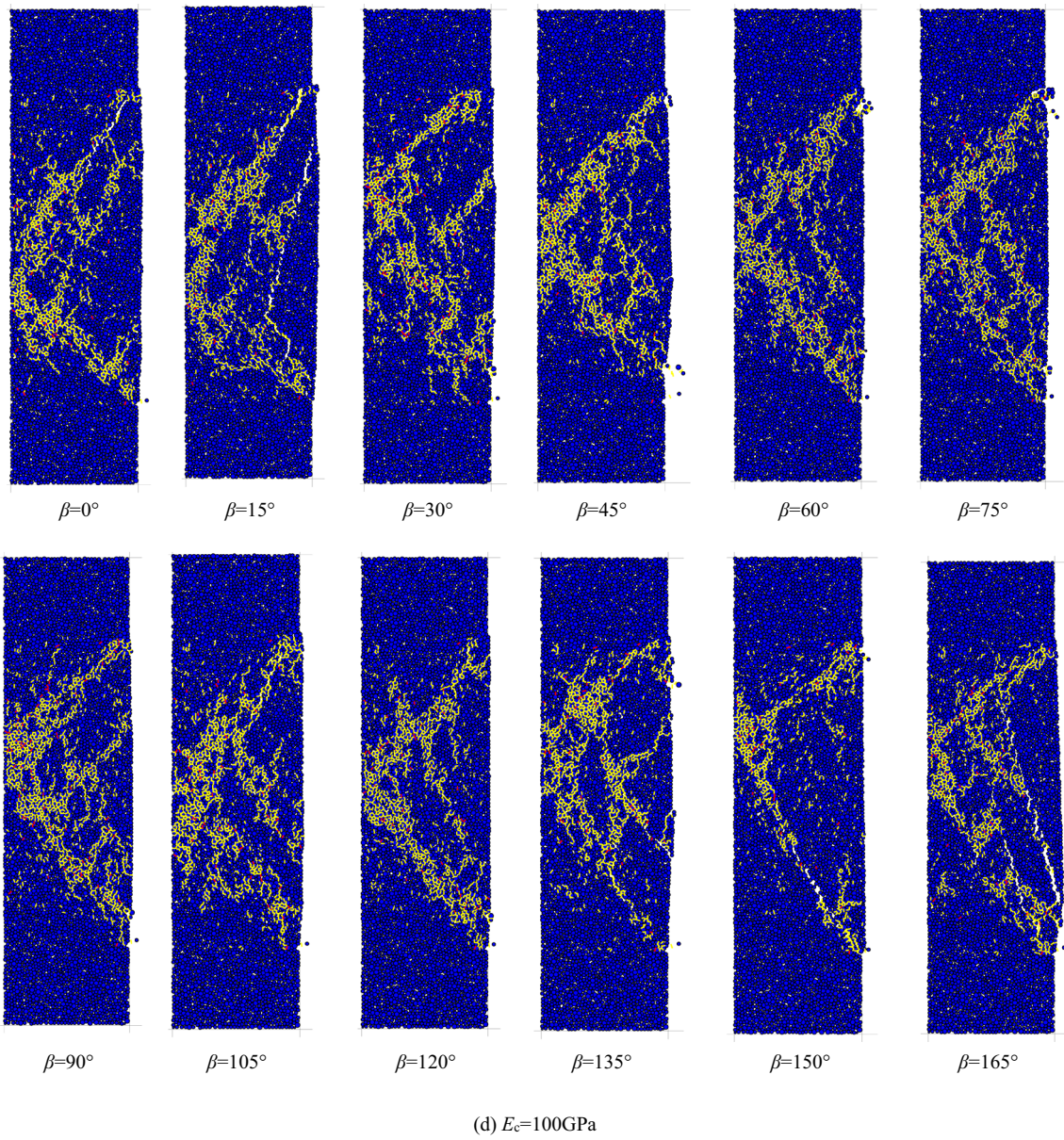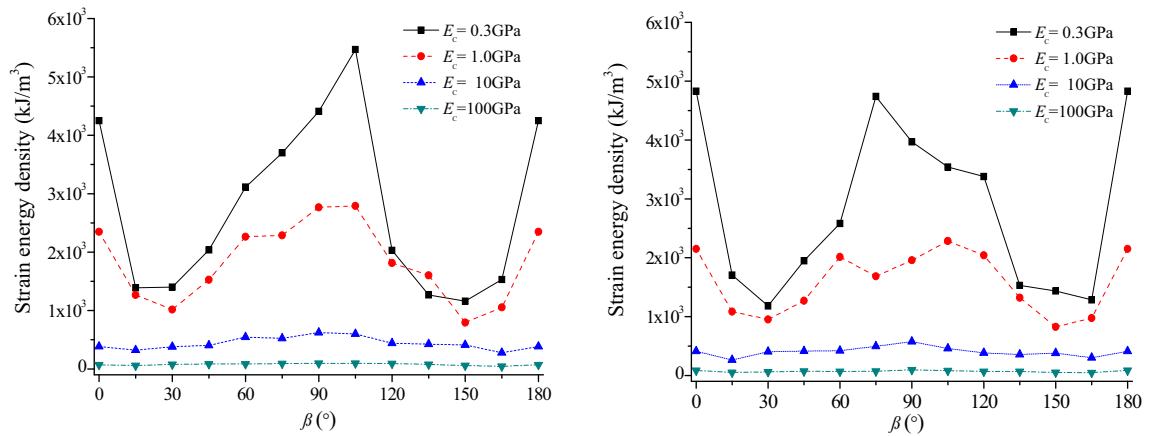
(d) E_c=100GPa

Fig. 12 (continued)

Fig. 13 Relationship between SED and structural plane orientations under different system stiffness, (a) for the roof and (b) floor
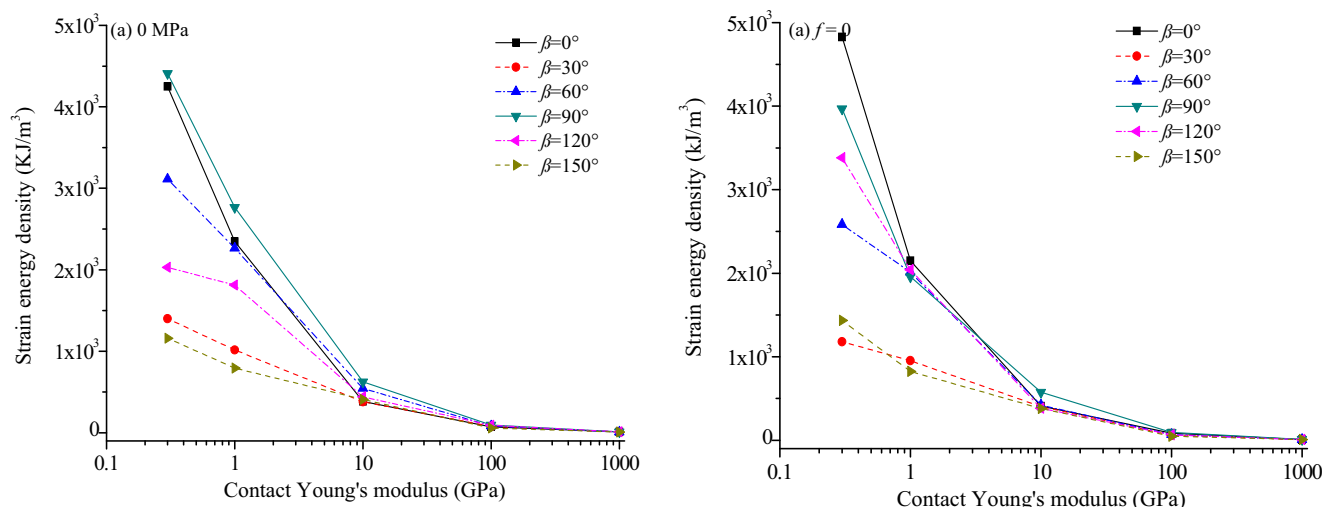
Fig. 14 Relationship between SED and contact Young's modulus for different structural plane orientations, (a) for the roof and (b) floor

Figure 12(b) shows the results of the numerical analysis when $E_c = 1$GPa. The main failure mode is also tensile, but the fracture is less well developed than when $\beta = 0°$ (180°). There are a few particle and fragment ejections, but the vertical fracture does not penetrate the whole rock mass. At $\beta = 15°$ and 165°, the failure mode was dominated by the structural planes, and tensile failure along the planes and buckling were much weaker. Some tensile cracks form crossing bedding planes in the rock mass. At $\beta = 30°$ and 150°, the main failure mode was also sliding along the bedding planes. At $\beta = 45°$ and 135° ($E_c = 0.3$GPa), there was both sliding along the planes and tensile failure crossing the planes. At $\beta = 60°$ and 120°, failure was dominated by the tensile and shear failure crossing the structural planes. At $\beta = 75°$ and 105°, the failure mode was mainly tensile with some shear fractures, which is similar the intact failure mode under the same environmental rock mass. At $\beta = 90°$, the failure was dominated by tensile fracturing and buckling independent of structural planes.

Figure 12(c) shows the results of the numerical analysis when $E_c = 10$GPa. With increasing SR between the environmental rock mass and bursting rock mass, fracturing is weaker and failure modes show some differences. At $\beta = 0°$ (180°), in addition to some small spalling and particle ejections near the excavation, there were some shear fractures which were not controlled by structures in the rock mass. At $\beta = 15°$ and 165°, the structures effect the failure mode; however, fractures do not penetrate the rock mass; At $\beta = 30°$ and 150°, or $\beta = 45°$ and 135°, the main failure mode was shear failure. Some shear fractures parallel the structure while others crossed it. At $\beta = 60°$ and 120°, most of the shear fractures crossed structural planes. At $\beta = 75°$ and 105°, failure was primarily shear fractures independent of the structure. At $\beta = 90°$, obvious tensile failures could be observed near the excavation surface and shear failure occurred in the rock mass.

Figure 12(d) shows the results of the numerical analysis when $E_c = 100$GPa. At $\beta = 0°$ (180°), no tensile failure was observed, and the main failure mode was shear
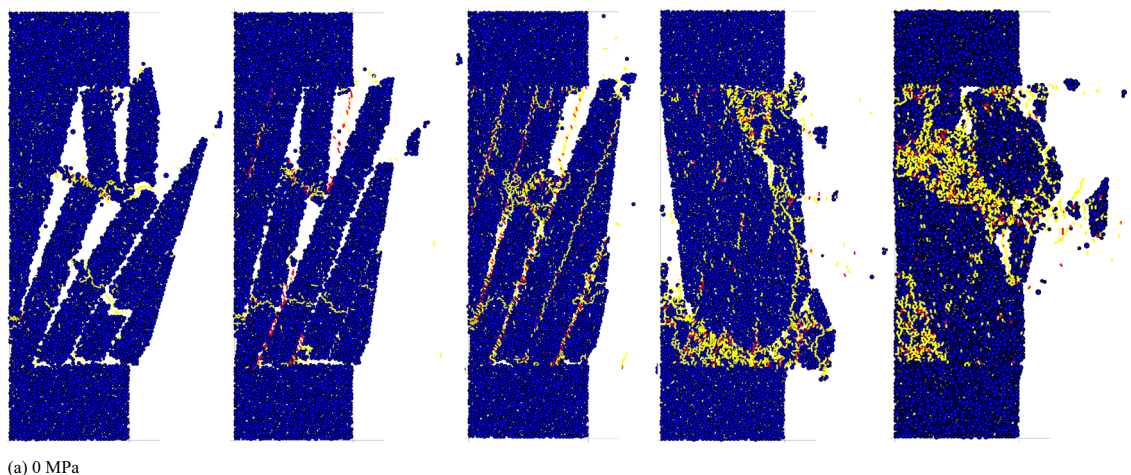

(a) 0 MPa

Fig. 15 Failure features of the rock mass with different bonding strengths ($\beta = 15°$ and $E_c = 0.3$ GPa)
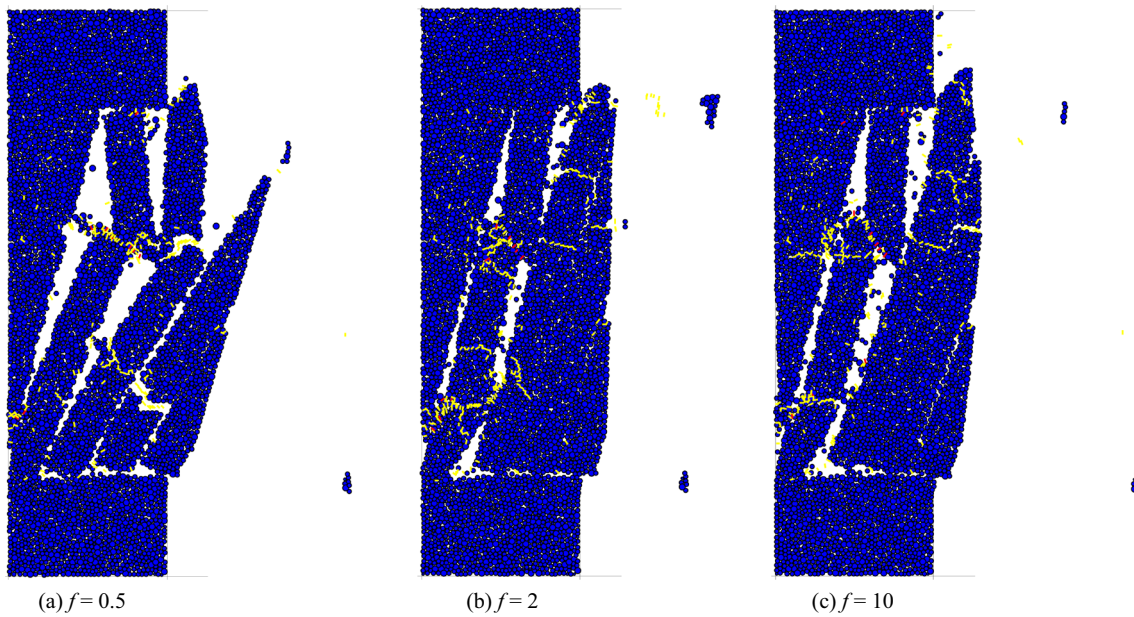
(a) $f = 0.5$ (b) $f = 2$ (c) $f = 10$

Fig. 16 Failure features of the rock mass with different friction coefficients ($\beta = 15°$ and $E_c = 0.3$ GPa)

fracturing with few particle ejections; At $\beta = 15°$ and 165°, the main failure mode was shear fracturing as well as some tensile fracturing along structural planes near the excavation surface; At $\beta = 30°$ and 150°, or $\beta = 45°$ and 135°, the main failure mode was shear fracturing. Some shear fractures are perpendicular to the structure. At $\beta = 60°$ and 120°, or $\beta = 75°$ and 105°, the failure mode was mainly shear fracturing independent of the rock structure, which was similar to the failure mode of intact rock under the similar SR. At $\beta = 90°$, no tensile failure was observed near the excavation surface, and shear failure not controlled by the structure occurred in the rock mass.

With increasing SR, the failure mode becomes more stable, and the influence of the structures on failure mode vanishes gradually. If the SR is high enough, the failure modes of the rock mass with various orientated discontinuities are similar to the failure mode for massive rock under the corresponding SR; When the SR is very low, failure of the rock mass with vertical or steeply inclined structural planes is dominated by spalling along the structures and buckling. When the structures are flatter, spalling is weakened and shearing along the structures becomes more significant. When the structures are flat or near flat, rock failure is dominated by spalling and buckling independent of structures and is always violent.
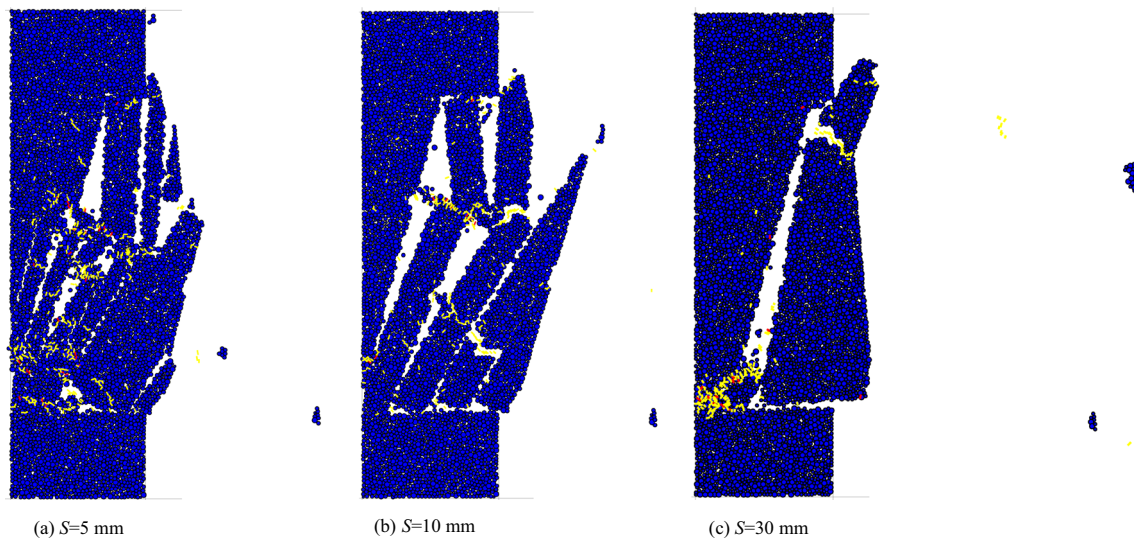

(a) $S = 5$ mm   (b) $S = 10$ mm   (c) $S = 30$ mm

Fig. 17 Failure features of the rock mass with different spacings ($\beta = 15°$ and $E_c = 0.3$ GPa)
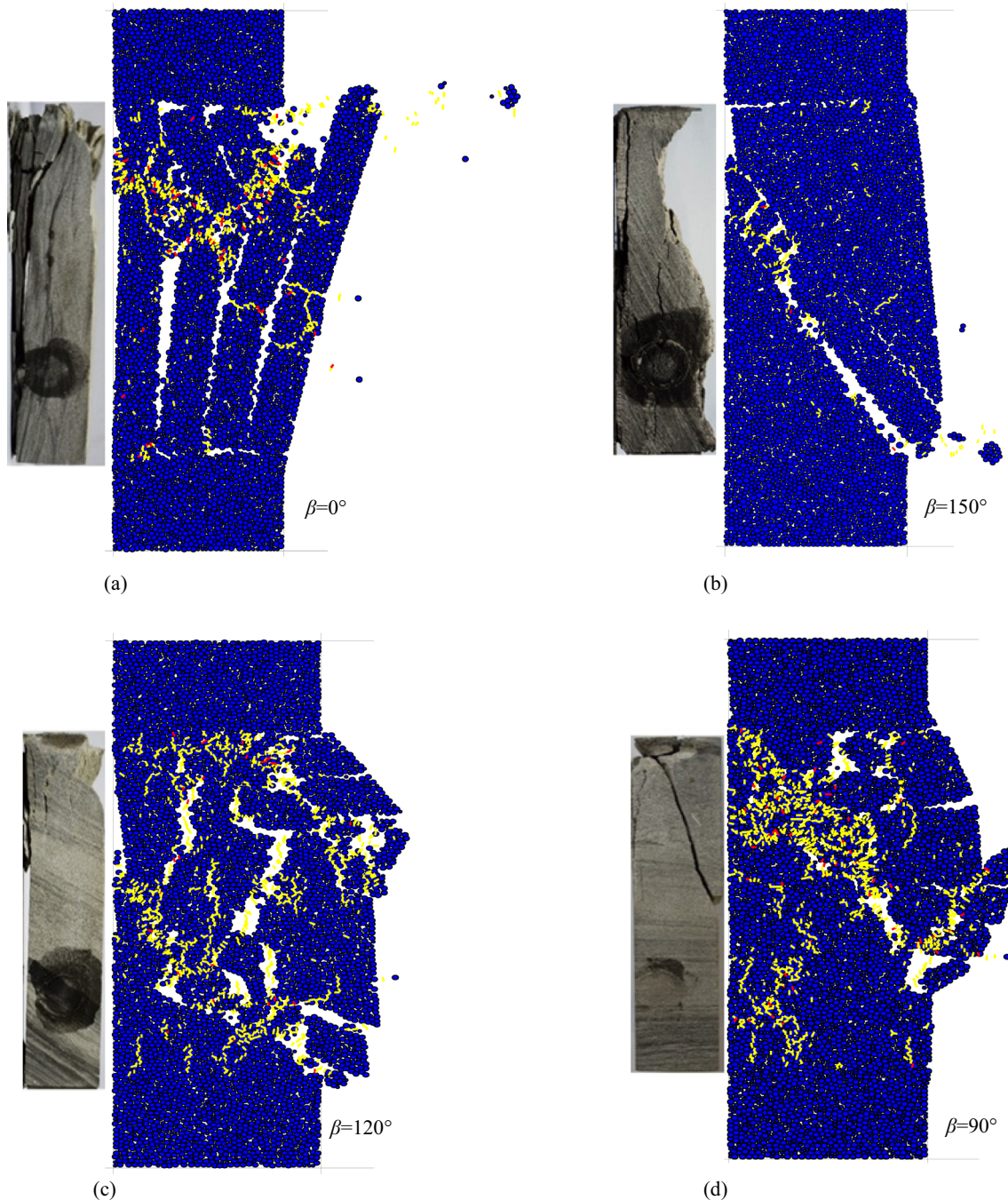
Fig. 18 Failure modes of experimental and numerical tests, (a~d) corresponding dip angles are 0°, 30°, 60°, and 90°, respectively

Energy release from the roof and floor

The SEDs from the environmental rock mass are plotted in Figs. 13 and 14 for each test on the bursting rock mass with different structural orientations under different SRs.

From the perspective of the energy release from the surrounding rock (roof and floor): (1) as the SR increases, the SED from the surrounding rock decreases, and the variance in SED with different discontinuity orientations also decreases (as shown in Fig. 13).

These results correspond to the gradual decrease in failure violence and influence the failure mode; (2) when the SR is lowest, the SED from the surrounding rock for steep* and moderately inclined ($\beta = [15°, 45°]$ & $[135°, 165°]$) structures in the rock mass are lower, and flatter structures ($\beta = [75°, 105°]$) correspond to higher SED values; (3) for horizontal ($\beta = 90°$) and vertical ($\beta = 0°$) structures, SED variation with the SR is more sensitive. For steep ($\beta = 30°, 150°$) and medium discontinuities ($\beta = 60°, 120°$), the sensitivity is lower.

*Note: (1) steep, $\beta = [15°, 30°]$ & $[150°, 165°]$; (2) moderately inclined (medium discontinuities), $\beta = [45°, 60°]$ & $[120°, 135°]$; (3) flatter, $\beta = [75°, 105°]$; (4) horizontal, $\beta = 90°$; (5) vertical, $\beta = 0°$.

Discussion

In previous studies, structural plane properties were set constant numerical tests. However, the normal and shear strength ('n_bond' and 's_bond') of each of the planes, friction coefficient ('fric') of the balls at the surface of the planes, and distances ('spacing') between two neighboring structural planes all have an influence on the failure mode.

Influence of the bonding strength

In the PFC model, the different (0, 10, 30, 50, and 80 MPa) normal and shear strengths were set to make different bonding strengths. In addition, β and E_c were set as $15°$ and 0.3 GPa, respectively. Figure 15 shows the failure features of the rock mass with different structural plane bonding strengths. Tensile failure of structural planes was predominant at lower boding strengths. If bonding strength is larger than 50 MPa, the main failure modes are not controlled by the structural plane.

Influence of the friction coefficient

Figure 16 shows the failure features of the rock mass with different friction coefficients. The tensile failure modes of rock mass are nearly unchanged as the friction coefficient rises. However, the friction force will affect the intensity of the tension. A larger friction coefficient will restrain the tensile force, especially at the rock mass boundary.

Influence of the spacing

Figure 17 shows the failure features of the rock mass with different spacings between structural planes. The rock mass was more broken at smaller spacings, and bulking was more obvious. If the spacing was 30 mm, tensile fracturing and bulking presented with enough stress.

Comparison between experimental and numerical simulation

Figure 18 shows the experimental failure modes and the corresponding numerical results ($E_c = 0.3$GPa). The experimental failure modes are not exactly the same as the numerical tests, because the bedding planes in the specimens are inhomogeneous and some random interlayers exists in the bedding. However, laboratory and numerical tests both proved that a lower SR corresponds to a larger probability or stronger strain burst intensity. Additionally, the variable of the above numerical tests was only the dip angle and other parameters were kept unchanged. If the micro-parameters of the specimen and structural plane were modified according to the specific specimen, the numerical results could correspond to the lab test, but this was not the purpose of this study.

Conclusions

Laboratory strain burst tests on dolomite specimens with different stiffnesses and sandstone with four different bedding plane dip angles as well as numerical analyses of rock mass strain burst with different structures have been carried out to study the effect of stiffness on strain burst. Specific conclusions are as follows:

(1) Strain burst intensity is larger in a more flexible system environment and lower SR corresponds to a larger probability of strain burst;
(2) With increasing SR, failure mode tends to be more stable, and the influence of structures on the failure modes vanishes gradually. In addition, the SED from the surrounding rock decreases with increasing SR.
(3) For the lowest SR, the SED from the surrounding rock is lower for steep and medium structures ($\beta = [15°, 45°]$ & $[135°, 165°]$). Additionally, flatter structures ($\beta = [75°, 105°]$) correspond to higher SED.
(4) For vertical ($\beta = 0°$) and horizontal ($\beta = 90°$) structures, variations in SED are more sensitive to SR. For steep ($\beta = 30°, 150°$) and medium discontinuities ($\beta = 60°, 120°$), the sensitivity is lower.

References

Aglawe JP (1999) Unstable and violent failure around underground openings in highly stressed ground. PhD thesis. Kingston, Ontario: Queen's University

Andreev GE (1995) Brittle failure of rock materials: test results and constitutive models, A.A. Balkema

Blake W (1972) Rock-burst mechanics. Q Colo Sch Mines; (United States) 67:1

Brady BHG, Brown ET (1981) Energy changes and stability in underground mining: design applications of boundary element methods. Trans Inst Min Metall 90:61–68

Cho N, Martin CD, Sego DC (2007) A clumped particle model for rock. Int J Rock Mech Min Sci 44(7):997–1010

Cook NGW (1965) A note on rockbursts considered as a problem of stability

He M, Miao J, Feng J (2010) Rock burst process of limestone and its acoustic emission characteristics under true-triaxial unloading conditions. Int J Rock Mech Min Sci 47(2):286–298

He M, Xia H, Jia X, Gong W, Zhao F, Liang K (2012a) Studies on classification, criteria and control of rockbursts. J Rock Mech Geotech Eng 4(2):97–114

He MC, Nie W, Zhao ZY, Guo W (2012b) Experimental investigation of bedding plane orientation on the rockburst behavior of sandstone. Rock Mech Rock Eng 45(3):311–326

Hedley DGF (2002) Rockburst handbook for Ontario hardrock mines

Hoek E (2008) Practical rock engineering. Environ Eng Geosci 14(1):55–57

Hucka V, Das B (1974) Brittleness determination of rocks by different methods. Int J Rock Mech Min Sci Geomech Abstr 11(10):389–392

Kaiser P, Tannant D, Mccreath DR (1996) Drift support in burst-prone ground. Proc Natl Acad Sci U S A 72(10):3863–3867

Kaiser PK, Tang CA (1998) Numerical simulation of damage accumulation and seismic energy release during brittle rock failure—part II: rib pillar collapse. Int J Rock Mech Min Sci 35(2):123–134

Kias EMC, Gu R, Garvey R, Ozbay U (2011) Modeling unstable rock failure during a uniaxial compressive strength test. Illinois Register

Kulatilake PHSW, Malama B, Wang J (2015) Physical and particle flow modeling of jointed rock block behavior under uniaxial loading. Int J Rock Mech Min Sci 38(5):641–657

Ortlepp W, Stacey T (1994) Rockburst mechanisms in tunnels and shafts. Tunn Undergr Space Technol 9(1):59–65

Salamon MDG (1970) Stability, instability and design of pillar workings. Int J Rock Mech Min Sci Geomech Abstr 7(6):613–631

Singh SP (1988) Burst energy release index. Rock Mech Rock Eng 21(2): 149–155

Stavrogin AN, Tarasov B, Fairhurst C (2001) Experimental physics and rock mechanics (Results of Laboratory Studies)

Tan YSC (1995) An analysis of present-day regional tectonic stress field and crustal movement trend in China. J Geom 1:12 (in Chinese)

Yong MT, Ming CK, Juang CH (2006) An experimental investigation of the failure mechanism of simulated transversely isotropic rocks. Int J Rock Mech Min Sci 43(8):1163–1181

Zhang J, Fu B, Li Z, Song S, Shang Y (2011) Criterion and classification for strain mode rockbursts based on five-factor comprehensive method. Harmonising Rock Engineering and the Environment